ANALYTICAL SOLUTIONS AND OPTIMAL PERTURBATIONS IN ACCELERATING AND DECELERATING LAMINAR CHANNEL FLOWS

Alec J. Linot
Department of Mechanical
and Aerospace Engineering
University of California, Los Angeles
CA 90095, USA
aleclinot@gmail.com

Peter J. Schmid
Department of Mechanical Engineering
King Abdullah University of
Science and Technology
23955 Thuwal, Saudi Arabia
peter.schmid@kaust.edu.sa

Kunihiko Taira
Department of Mechanical
and Aerospace Engineering
University of California, Los Angeles
CA 90095, USA
ktaira@seas.ucla.edu

ABSTRACT

The stability of unsteady flows can vary drastically from that of steady flows; however, the mechanisms leading to the changes in stability often remain unclear. Here, we probe these mechanisms by isolating the effects of acceleration and deceleration. We do this by studying the stability of exponentially decaying accelerating and decelerating wall motion in a planar domain. For studying the stability of unsteady laminar flow profiles, we find the exact solutions and perform nonmodal stability analysis about them. Notably, standard linear stability methods do not properly account for the transient nature of the unsteady base flows considered here. First, to find the laminar profiles, we derive an analytical solution for laminar planar flows with arbitrary wall motion. Then, we study the stability of this analytical solution by computing the transient, nonmodal growth of perturbations in the linearized equations.

In this study, we find that perturbations in the accelerating flow never grow larger than perturbations to a constant flow, while perturbations in the decelerating flow exhibit massive amplification. For example, at a Reynolds number of $Re = 800$, perturbations in the decelerating flow can grow $\mathscr{O}(10^6)$ times larger than perturbations to a constant flow. As we vary the Reynolds number and deceleration rate, the maximum amplification grows and, at a high deceleration rate, scales exponentially with the Reynolds number. This increased amplification is caused by a transition from spanwise perturbations leading to the maximum growth to streamwise perturbations leading to the maximum growth. Furthermore, we show the evolution of the optimal perturbations. At sufficiently high rates of deceleration, the optimal perturbation grows through the Orr mechanism (also known as a down-gradient Reynolds stress mechanism). Notably, the decelerating case can sustain growth via the Orr mechanism for long periods of time, whereas constant and accelerating flows only grow via this mechanism for short periods of time, which results in a massive difference in amplification between the cases. We then simulate the evolution of the perturbation in a direct numerical simulation – showing the relevance of this mechanism even when nonlinearity is present. Finally, we end by showing that there is an optimal timing to the perturbation that occurs near when the real part of the leading eigenvalue of the instantaneous linear operator becomes positive.

Laminar solutions for planar flow

To investigate the growth of perturbations about the laminar base profile, we first need the laminar velocity profile. Laminar solutions exist for the motion in one direction with impulsively starting wall motion, periodic wall motion (Schlichting & Gersten, 2017), and arbitrary periodic wall motion (Daidzic, 2022), but *not* for arbitrary wall motion. To find solutions for arbitrary motion in a channel with two infinite directions, we seek laminar solutions $U(y,t)$ that only depend on the wall-normal coordinate and time. Upon substitution of $U(y,t)$ into the nondimensionalized Navier-Stokes equations, we obtain

$$\frac{\partial U}{\partial t} = \frac{1}{Re}\frac{\partial^2 U}{\partial y^2} \tag{1}$$

with boundary conditions $U(y=\pm 1,t) = \pm g_c(t)$ and initial condition $U(y,t=0) = h_c(y)$. Equation (1) represents the one-dimensional heat equation, a linear equation that, together with boundary and initial conditions, can be solved using Fourier analysis and the superposition principle.

In particular, we seek odd functions $U(y,t) = -U(-y,t)$, motivating the use of a sin basis. These basis functions vanish at the walls for $y \in [-1,1]$, which prompts us to pose the flow solution in the form

$$U(y,t) = f_c(y,t) + \frac{Re}{6}\frac{dg_c}{dt}(y^3 - y) + g_c(t)y \tag{2}$$

to accommodate the stated boundary conditions. Inserting this expression into Eq. (1) yields an equation for f_c according to

$$\frac{\partial f_c}{\partial t} + \frac{Re}{6}\frac{d^2 g_c}{dt^2}(y^3 - y) = \frac{1}{Re}\frac{\partial^2 f_c}{\partial y^2}, \tag{3}$$

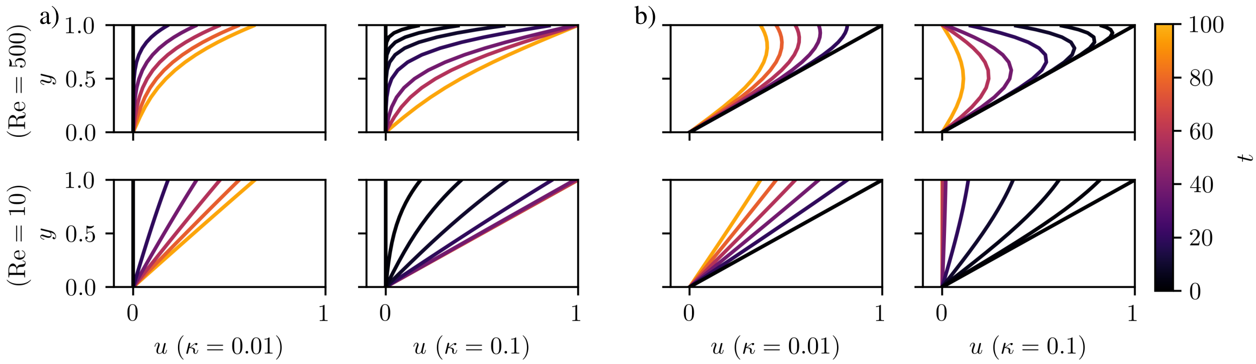

Figure 1: Laminar profiles for (a) accelerating and (b) decelerating flows at various Re and κ (noted in the figure).

with boundary conditions $f_c(y=\pm 1,t)=0$ and initial condition $f_c(y,0)=h_c-(Re/6)(dg_c/dt)|_0(y^3-y)-g_c(0)y$.

We next express f_c in a Fourier-sine expansion following $f_c(y,t)=\sum_{n=1}^{\infty}\hat{f}_{c,n}(t)\sin(n\pi y)$. Substitution of the Fourier expansion into Eq. (3) and taking the inner product with $\sin(m\pi y)$, we obtain an ordinary differential equation for the time-dependent Fourier coefficients $\hat{f}_{c,m}$ given by

$$\frac{d\hat{f}_{c,m}}{dt}=-\frac{2Re(-1)^m}{(\pi n)^3}\frac{d^2 g_c}{dt^2}-a_m\hat{f}_{c,m}, \tag{4}$$

where $a_m=(\pi m)^2/Re$. Solving Eq. (4) results in

$$\hat{f}_{c,m}=e^{-a_n t}\left(-\frac{2Re(-1)^n}{(\pi n)^3}\int_0^t e^{a_n t'}\frac{d^2 g_c(t')}{dt^2}dt'+C_1\right) \tag{5}$$

with C_1 following from imposing the initial condition. Finally, by combining $\hat{f}_{c,n}$ with Eq. (2) and evaluating C_1 for simple shear initial conditions ($h_c=g_c(0)y$), we find the time-dependent laminar profile

$$U(y,t)=\frac{Re}{6}\frac{dg_c}{dt}(y^3-y)+g_c(t)y$$
$$+\sum_{n=1}^{\infty}b_n e^{-a_n t}\left(\int_0^t e^{a_n t'}\left.\frac{d^2 g_c}{dt^2}\right|_{t'}dt'+\left.\frac{dg_c}{dt}\right|_0\right)\sin(n\pi y), \tag{6}$$

where $b_n=-2Re(-1)^n/(\pi n)^3$. A more detailed description of this derivation can be found in Linot *et al.* (2023*a*).

Equipped with this solution, we proceed with our specific flows of interest – an exponentially decaying, accelerated or decelerated flow. The time-varying boundary condition for the accelerated case is $g_c(t)=1-e^{-\kappa t}$, and for the decelerated case is $g_c(t)=e^{-\kappa t}$. These flows are interesting because they isolate the effects of acceleration and deceleration, unlike a pulsatile flow, which would experience both regimes. Furthermore, this type of boundary condition can be seen in both internal flows, like the start-up and stopping of pipe flow (Greenblatt & Moss, 2004), and external flows, including accelerating/decelerating vehicles. Furthermore, the stability of this flow has been investigated using the energy method (Conrad & Criminale, 1965).

This flow is parameterized by both the Reynolds number Re and the nondimensional acceleration/deceleration scale κ. This parameter is inversely proportional to the timescale associated with the wall motion. Consequently, solutions to our unsteady analysis are characterized by two timescales: (1) the Reynolds number Re gives the timescale over which fluid in the channel reacts to wall motion, and (2) the parameter κ determines the timescale over which the wall motion occurs. In

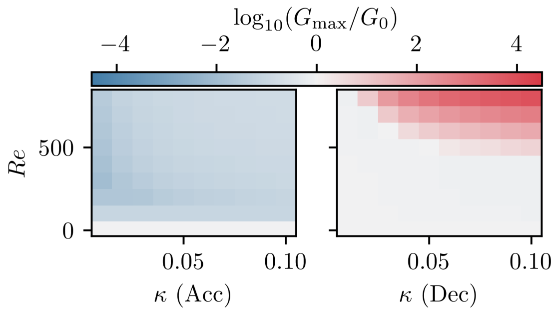

Figure 2: The maximum growth (in time and wavenumbers) $G_{\max}$ relative to a constant laminar profile for accelerating and decelerating flows at various Re and κ with $t_0=0$. Acceleration and deceleration are denoted in the figure.

Fig. 1, we show the time evolution of the laminar profiles for multiple values of Re and κ, both for acceleration and deceleration. At low Re and κ, acceleration, as well as deceleration, exhibit nearly linear, simple shear flow since the timescale of wall motion is slower than the timescale over which the flow reacts to this motion. At higher Re and κ, both the accelerating and decelerating velocity profiles exhibit high curvatures near the wall at early times, before approaching the long-time simple shear or zero flow profiles. Notably, the sign of the curvature differs between acceleration and deceleration, which will lead to much different behavior of the perturbations superimposed on these velocity profiles.

Nonmodal growth

Given the expression for the laminar profiles, we investigate next the stability of these flows. In particular, we are interested in the growth of small perturbations governed by the linearized equations of motion

$$\frac{\partial \mathbf{q}}{\partial t}=-\mathrm{i}\mathscr{L}\mathbf{q}. \tag{7}$$

Here, $\mathbf{q}$ is the state vector consisting of the wall-normal perturbation velocity and the wall-normal perturbation vorticity in Fourier space (in x and z) $\mathbf{q}(y,t,\alpha,\beta)=[\hat{u}_y,\hat{\eta}]$, and $\mathscr{L}$ represents the Navier-Stokes equations linearized about the time-dependent laminar base profile; the reader is referred to Schmid & Henningson (2001) for more details. Using the linearized equations of motion, we can compose the fundamental solution operator $A(t;t_0)$ as a compound product of ma-

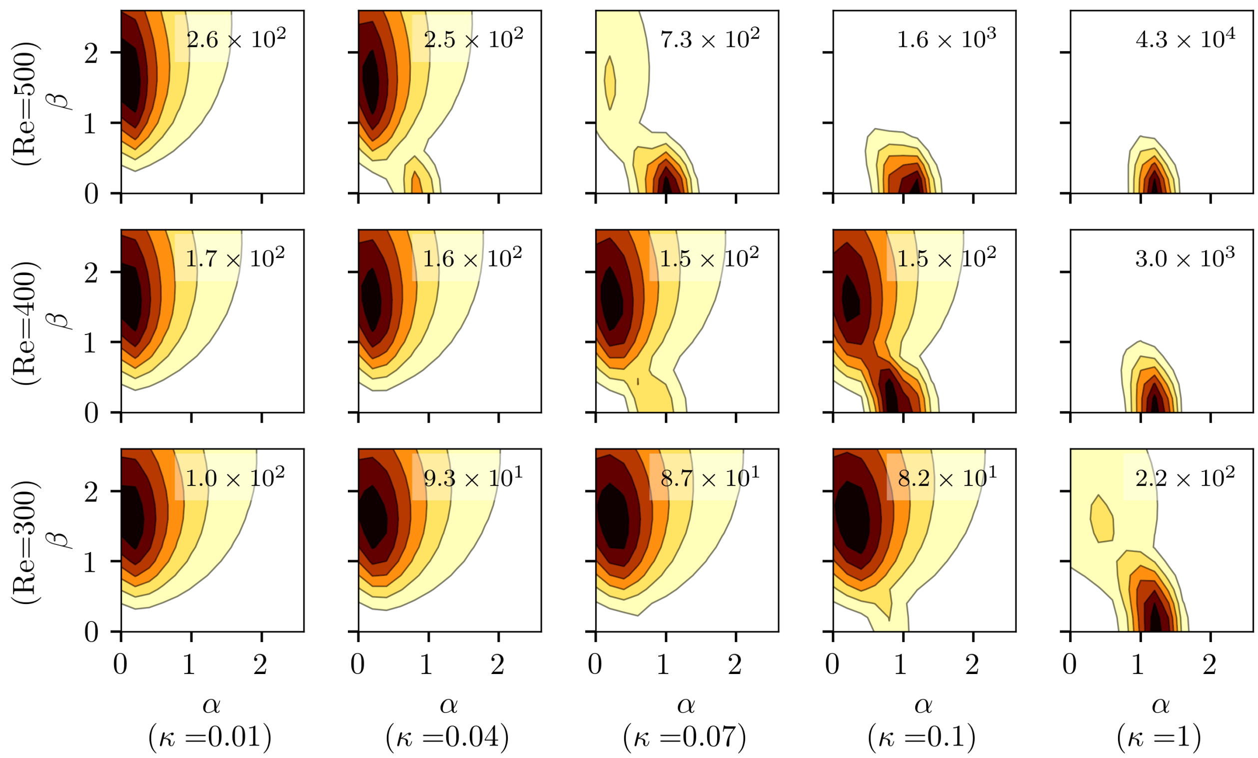

Figure 3: Maximum amplification of perturbations $\max_t G(t)$ for decelerating WDF at different wavenumbers and deceleration rates (denoted in the figure) with $t_0 = 0$. Each plot is normalized by the maximum amplification over all wavenumbers, which is reported in the top right.

trix exponentials, i.e., $A(t;t_0) = \Pi_{j=1}^{N} e^{-\mathrm{i}\mathscr{L}(j\Delta t + t_0)\Delta t}$ (we suppress the α and β dependency of A for compactness). This operator maps the perturbation $\mathbf{q}_0 = \mathbf{q}(y,t_0)$ forward in time $\mathbf{q}(y,t) = A(t;t_0)\mathbf{q}_0$.

Based on this solution operator, we determine the maximum possible amplification of any perturbation as

$$G(t;\alpha,\beta,Re,\kappa,t_0) = \max_{\mathbf{q}_0 \neq 0} \frac{||\mathbf{q}(t)||_E^2}{||\mathbf{q}_0||_E^2} = \max_{\mathbf{q}_0 \neq 0} \frac{||A(t;t_0)\mathbf{q}_0||_E^2}{||\mathbf{q}_0||_E^2}, \tag{8}$$

where $\|\cdot\|_E$ denotes a properly defined energy norm. This amplification signifies the largest growth achievable by any unit norm perturbation as it is propagated forward to time t. We compute $G(t)$ using the singular value decomposition of $A(t;t_0)$ (appropriately weighted). The maximum gain $G(t)$ is given by the principal singular value and the associated optimal perturbation corresponds to the right principal singular vector.

Figure 2 shows the maximum growth $G_{\max} = \max_{t,\alpha,\beta} G$ as we vary Re and κ in the accelerating and decelerating flows for perturbations at $t_0 = 0$ (G_0 denotes the maximum growth for a constant wall velocity). The maximum gain for the accelerating case never exceeds that of the constant laminar flow. In contrast, the decelerating flow exhibits orders of magnitude larger growth at high values of Re and κ. Notably, at these higher parameter values, the maximum gain exhibits a 10^{Re} scaling, which has also been observed in oscillatory flows (Biau, 2016; Xu *et al.*, 2021).

To investigate the cause of this growth, we next focus on the growth of all wavenumbers near the transition Reynolds numbers ($\sim$ 300-500) for the decelerating flow. Figure 3 displays the maximum amplification versus the streamwise and spanwise wavenumber, α and β, as we vary Re and the deceleration rate κ. At low Re and κ, the largest optimal perturbation is predominantly a spanwise perturbation with $[\alpha,\beta] \approx [0, 1.6]$. This agrees well with the wavenumbers of the optimal perturbation for both the constant flow (Reddy & Henningson, 1993) and for the accelerating flow (not shown). However, upon increasing Re and κ, the dominant optimal perturbation transitions from a spanwise perturbation to a streamwise perturbation with $[\alpha,\beta] \approx [1.2, 0]$. This gradual transition from spanwise dominant perturbations to streamwise dominant perturbations highlights that deceleration alone is not enough to trigger massive growth. Instead, there is a boundary of Re and κ passed which large growth may be triggered. Additionally, there must be a fundamental mechanistic change in the evolution of perturbations at these higher values that allows streamwise perturbations to grow larger than the spanwise perturbations.

We investigate this shift in preferred perturbation by considering the time evolution of the optimal perturbation required to achieve the peak maximum amplification at wavenumbers $[\alpha,\beta] \approx [1.2, 0]$, deceleration rate $\kappa = 0.1$, and Reynolds number $Re = 500$. The initial condition that results in this peak can be computed by finding the principle left singular vector $\mathbf{v}_1$ of $A(t_{\max};0)$, where $t_{\max} = \operatorname{argmax}_t G(t)$. Then we evolve this perturbation forward in time through the linearized equations of motion $\mathbf{v}(t) = A(t;0)\mathbf{v}_1$. Figure 4 shows the energy growth for the optimal perturbations in a decelerating and a constant flow, along with the shape of the perturbations as they evolve in time. Both decelerating and constant flow have very similar initial perturbations that exhibit initial growth in energy, followed by asymptotic decay. However, at longer times, the shape of the perturbation in a decelerating flow begins to differ from that of the constant flow, which induces drastic

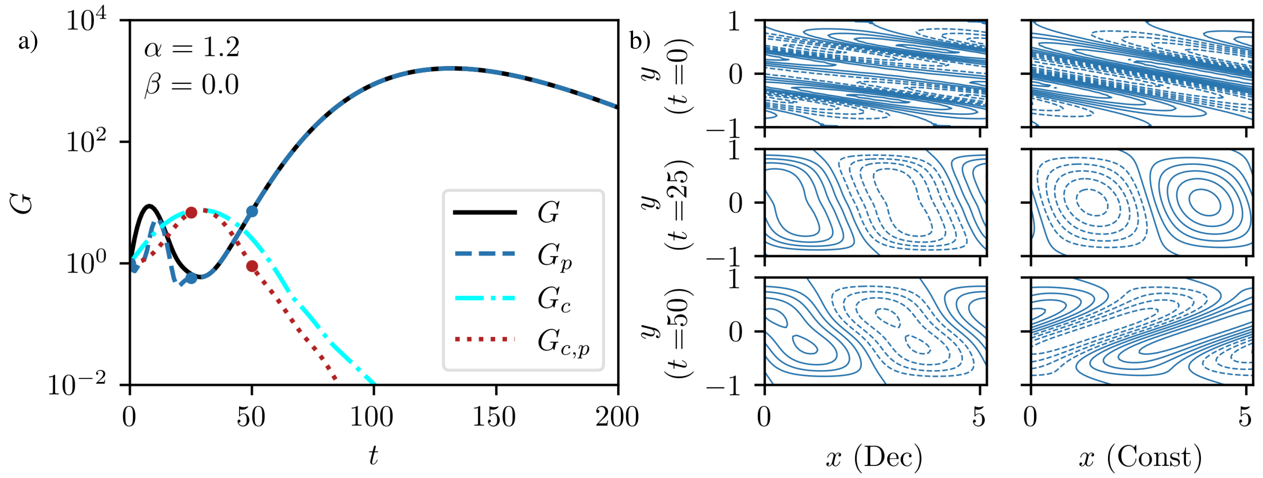

Figure 4: (a) time evolution of the maximum amplification G for decelerating flow, the energy of the optimal perturbation for decelerating flow G_p, the maximum amplification for constant flow G_c, and the energy of the optimal perturbation for constant flow $G_{c,p}$. All results are at $Re = 500$, $\kappa = 0.1$, $\alpha = 1.2$, $\beta = 0$, and $t_0 = 0$. The stream function of the optimal perturbations at the times indicated by the dots in (a) are shown in (b).

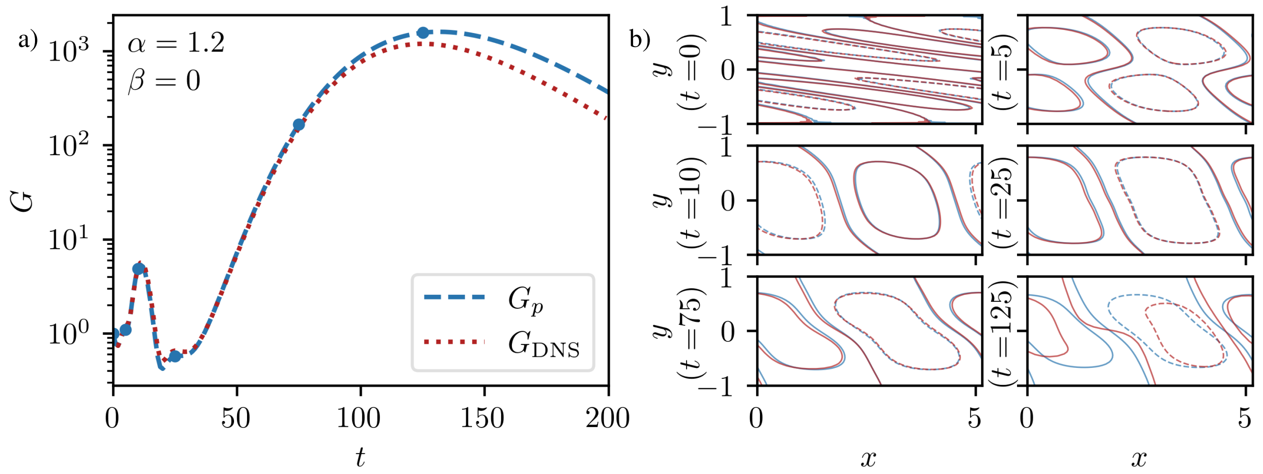

Figure 5: (a) time evolution of the energy of the optimal perturbation for decelerating flow G_p and of the optimal perturbation in a DNS G_{DNS} at $Re = 500$, $\kappa = 0.1$, $\alpha = 1.2$, $\beta = 0$, and $t_0 = 0$. The stream function of the optimal perturbations (in blue) and the DNS (in red) at the times indicated by the dots in (a) are shown in (b).

energy amplification. The streamfunction of the perturbation maintains alignment against the shear in the decelerating case, which provokes a strong increase in energy via the Orr mechanism (Orr, 1907), which Butler & Farrell (1992) refer to as a down-gradient Reynolds stress mechanism.

Direct numerical simulation of perturbations

Next, we show the relevance of the evolution of this perturbation in a direct numerical simulation (DNS) of the full Navier-Stokes equations, again at $Re = 500$ and $\kappa = 0.1$. To perform the DNS, we use a Fourier–Chebyshev pseudo-spectral code implemented in Python (Linot *et al.*, 2023*b*,*c*), that is based on the Channelflow code developed by Gibson (2012); Gibson *et al.* (2021). To satisfy the decelerating boundary condition at every timestep we integrate forward in time using the Spalart-Moser Runge-Kutta (SMRK2) scheme (Spalart *et al.*, 1991). This scheme treats the linear term implicitly and the nonlinear term explicitly, and is a multistage scheme, so it does not require the use of flowfields on previous timesteps. This would be an issue, as the boundary condition changes every step. We simulate the flow using a grid of size $[N_x, N_y, N_z] = [32, 81, 2]$ with a timestep of $\Delta t = 0.01$. The initial condition for the DNS is $\mathbf{u} = \mathbf{U} + \mathbf{u}'$, where we reduce the magnitude of the optimal perturbation such that the initial energy ratio is $||\mathbf{u}'||_E^2/||\mathbf{U}||_E^2 \approx 10^{-7}$.

Figure 5 compares the energy and shape of the optimal perturbation in the DNS to the linearized equations. The two energy curves match well until around $t \approx 125$, where the DNS begins to decrease in energy more rapidly. This slight variation occurs when the ratio of energy is $||\mathbf{u}'||_E^2/||\mathbf{U}||_E^2 \approx 0.09$ – caused by both the growth in the perturbation and the decay in the energy of the laminar profile. At this point, the perturbation is large enough that nonlinear effects can play a role in the dynamics. Figure 5b shows the evolution of the perturbation. As expected, the DNS results match the optimal perturbation until $t \approx 75$, while at $t \approx 125$ we see that perturbation begins to become distorted due to nonlinear effects.

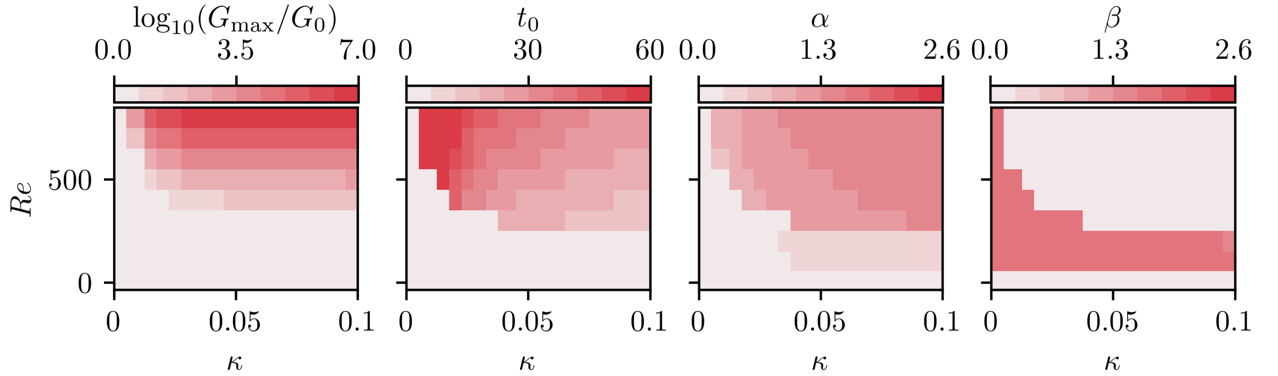

Figure 6: The maximum amplification G, the perturbation time t_0, and the wavenumbers $[\alpha, \beta]$ at which the maximum perturbation is achieved for decelerating flow at various Re and κ.

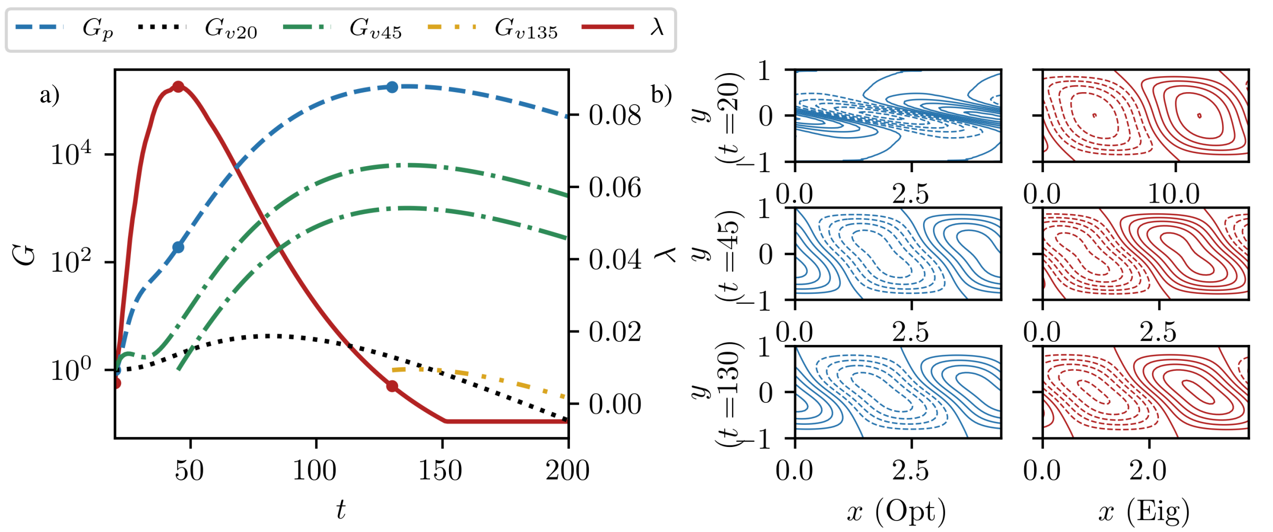

Figure 7: (a) energy of the optimal perturbation G_p and energy of the eigenvectors G_{vT} of the instantaneous linear operator at various times T as these perturbations are evolved forward through the linearized equations. Note, that the eigenvector corresponds to the profile at time T, but the time at which it is applied to the flow is where the line begins. Additionally, (a) shows the largest real eigenvalue λ for decelerating flow at $Re = 500$, $\kappa = 0.1$, $\alpha = 1.2$, $\beta = 0$, and $t_0 = 20$. (b) gives the stream function of the optimal perturbation (in blue) and the eigenvectors (in red) at times indicated by the dots in (a).

Optimal perturbation timing

Thus far, we have only considered perturbations applied to accelerating and decelerating flows at the initial change in the wall motion, however, the maximum amplification can vary if we delay when the perturbation is applied. In this section, we investigate the effect of allowing this time to vary for decelerating flows. We perform this analysis by now sweeping over α, β, and t_0 at fixed κ and Re values to compute $G_{\max} = \max_{t,\alpha,\beta,t_0} G$. Figure 6 shows this maximum growth, along with the parameters at which it is achieved.

Similar to perturbing at $t_0 = 0$, we see that there is a large increase in growth that coincides with a transition from spanwise dominant to streamwise dominant structures. However, by allowing t_0 to vary the area over which this growth becomes prominent increases. At low κ, the growth is larger when the perturbation is delayed, as this gives the profile more time to develop the curvature exhibited in Fig. 1b. As κ increases, the laminar profile develops faster resulting in a faster perturbation timing.

To better understand this timing, in Fig. 7 we show the optimal perturbation applied at the optimal timing along with the eigenvalues and eigenvectors of the instantaneous linear operator for $Re = 500$ and $\kappa = 0.1$. Notice, that the optimal perturbation timing happens around the same time as when the eigenvalue of the instantaneous linear operator becomes positive. However, the shape of the optimal perturbation at this time is much more anti-aligned with the flow and much smaller in the spanwise direction than the largest eigenvector at this time. As the optimal perturbation evolves it rotates, aligning with the shear, and matches the eigenvector associated with the peak in the eigenvalue curve. Then, the optimal perturbation continues to grow with this shape until the eigenvalue falls below zero, which coincides with the peak in the energy.

This highlights that both modal and nonmodal effects influence the evolution of the optimal perturbation. The optimal perturbation takes on a shape that grows into the eigenvector with the largest eigenvalue and then maintains that shape for continued growth until the eigenvalue falls below zero. In Figure 7, we highlight the importance of the optimal perturbation by also showing the energy growth of the eigenvector at times

$t = 20, 45$, and 135. Perturbing these eigenvectors at those times always results in much lower growth than the optimal perturbation. Furthermore, perturbing the flow with the eigenvector with the largest eigenvalue at the initial time also results in two orders of magnitude less growth than the optimal perturbation. Thus, the initial growth that the optimal perturbation exhibits before matching the leading eigenvector results in a large increase in growth that would not be seen if we only considered the leading eigenvector from standard linear stability analysis.

Conclusion

In this study, we demonstrated that perturbations in decelerating laminar flows experience a severe energy amplification, which does not appear in accelerating flows. At a low deceleration rate and Reynolds number, the decelerating flow behaves like the accelerating and constant flows. Upon increasing these values, we have demonstrated that there is an important transition in the mechanism of growth that causes streamwise perturbations to grow larger than spanwise perturbations. These streamwise perturbations grow in all cases at early times through the Orr mechanism, but only the decelerating flow exhibits larger growth through this mechanism because the streamfunction remains aligned against the shear for long periods of time. Notably, the perturbation also grows in such a way that it matches the eigenvector of the instantaneous linear operator with the largest eigenvalue, and the optimal perturbation time can be predicted when the eigenvalue first becomes positive. These results indicate it is important to damp anti-aligned streamwise structures to avoid transition in decelerating flows. We aim to further expand these results to a wider array of unsteady wall motion in the future, which is facilitated by our derivation of analytical solutions for arbitrary streamwise motion.

REFERENCES

Biau, Damien 2016 Transient growth of perturbations in Stokes oscillatory flows. *Journal of Fluid Mechanics* **794**, R4.

Butler, Kathryn M. & Farrell, Brian F. 1992 Three-dimensional optimal perturbations in viscous shear flow. *Physics of Fluids A: Fluid Dynamics* **4** (8), 1637–1650.

Conrad, Peter W. & Criminale, William O. 1965 The stability of time-dependent laminar flow: Parallel flows. *Z. Angew. Math. Phys.* **16** (2), 233–254.

Daidzic, Nihad E. 2022 Unified theory of unsteady planar laminar flow in the presence of arbitrary pressure gradients and boundary movement. *Symmetry* **14** (4).

Gibson, J. F. 2012 Channelflow: a spectral Navier-Stokes simulator in C++. *University of New Hampshire* (July), 1–41.

Gibson, J. F., F. Reetz, S. Azimi, Ferraro, A., Kreilos, T., Schrobsdorff, H., Farano, M., Yesil, A. F., Schütz, S. S., Culpo, M. & Schneider, T. M. 2021 Channelflow 2.0.

Greenblatt, David & Moss, Edward A. 2004 Rapid temporal acceleration of a turbulent pipe flow. *Journal of Fluid Mechanics* **514**, 65–75.

Linot, Alec J., Schmid, Peter J. & Taira, Kunihiko 2023*a* On the laminar solutions and stability of accelerating and decelerating channel flows. *arXiv preprint arXiv:2312.12701* .

Linot, Alec J., Zeng, Kevin & Graham, Michael D. 2023*b* PyChannel. `https://github.com/alinot5/PyChannel`.

Linot, Alec J., Zeng, Kevin & Graham, Michael D. 2023*c* Turbulence control in plane couette flow using low-dimensional neural ode-based models and deep reinforcement learning. *International Journal of Heat and Fluid Flow* **101**, 109139.

Orr, William M'F. 1907 The stability or instability of the steady motions of a perfect liquid and of a viscous liquid. part i: A perfect liquid. *Proceedings of the Royal Irish Academy. Section A: Mathematical and Physical Sciences* **27**, 9–68.

Reddy, Satish C. & Henningson, Dan S. 1993 Energy growth in viscous channel flows. *Journal of Fluid Mechanics* **252**, 209–238.

Schlichting, Hermann. & Gersten, Klaus. 2017 *Boundary-Layer Theory / by Hermann Schlichting (Deceased), Klaus Gersten.*, 9th edn. Berlin, Heidelberg: Springer Berlin Heidelberg.

Schmid, Peter J. & Henningson, Dan S. 2001 *Stability and Transition in Shear Flows*, *Applied Mathematical Sciences*, vol. 142. New York, NY: Springer New York.

Spalart, Philippe R, Moser, Robert D & Rogers, Michael M 1991 Spectral methods for the Navier-Stokes equations with one infinite and two periodic directions. *Journal of Computational Physics* **96** (2), 297–324.

Xu, Duo, Song, Baofang & Avila, Marc 2021 Non-modal transient growth of disturbances in pulsatile and oscillatory pipe flows. *Journal of Fluid Mechanics* **907**, R5.